



HAL
open science

Characterization of a Deglaciaded Sediment Chronosequence in the High Arctic Using Near-Surface Geoelectrical Monitoring Methods

Mihai O Cimpoiasu, Oliver Oliver Kuras, Harry Harrison, Paul B Wilkinson, Philip Meldrum, Jonathan E Chambers, Dane Liljestrand, Carlos Oroza, Steven K Schmidt, Pacifica Sommers, et al.

► **To cite this version:**

Mihai O Cimpoiasu, Oliver Oliver Kuras, Harry Harrison, Paul B Wilkinson, Philip Meldrum, et al.. Characterization of a Deglaciaded Sediment Chronosequence in the High Arctic Using Near-Surface Geoelectrical Monitoring Methods. *Permafrost and Periglacial Processes*, 2024, 35 (2), pp.157-171. 10.1002/ppp.2220 . hal-04621012

HAL Id: hal-04621012

<https://hal.science/hal-04621012v1>

Submitted on 22 Jun 2024

HAL is a multi-disciplinary open access archive for the deposit and dissemination of scientific research documents, whether they are published or not. The documents may come from teaching and research institutions in France or abroad, or from public or private research centers.






L'archive ouverte pluridisciplinaire **HAL**, est destinée au dépôt et à la diffusion de documents scientifiques de niveau recherche, publiés ou non, émanant des établissements d'enseignement et de recherche français ou étrangers, des laboratoires publics ou privés.



Distributed under a Creative Commons Attribution 4.0 International License

RESEARCH ARTICLE OPEN ACCESS

Characterization of a Deglaciaded Sediment Chronosequence in the High Arctic Using Near-Surface Geoelectrical Monitoring Methods

Mihai O. Cimpoiasu¹  | Oliver Kuras¹  | Harry Harrison¹ | Paul B. Wilkinson¹ | Philip Meldrum¹ | Jonathan E. Chambers¹  | Dane Liljestr nd² | Carlos Oroza² | Steven K. Schmidt³ | Pacifica Sommers³  | Trevor P. Irons⁴ | James A. Bradley^{5,6} 

¹Environmental and Engineering Geophysics, British Geological Survey, Keyworth, UK | ²University of Utah, Salt Lake City, Utah, USA | ³University of Colorado, Boulder, Colorado, USA | ⁴Montana Technical University, Butte, Montana, USA | ⁵Aix Marseille University, Universit  de Toulon, CNRS, IRD, MIO, Marseille, France | ⁶School of Biological and Behavioural Sciences, Queen Mary University of London, London, UK

Correspondence: Mihai O. Cimpoiasu (mcim@bgs.ac.uk)

Received: 11 May 2023 | **Revised:** 23 January 2024 | **Accepted:** 30 January 2024

Funding: This work was funded by the NSF-UKRI Signals in the Soil (Grants NE/T010967/1, NE/T010568/1, 1935651, 2015329, and 1935689), the NERC Covid Fund, and the European Union's Horizon 2020 (Grant 730938).

Keywords: Arctic soils | geoelectrical monitoring | resistivity tomography | soil evolution | soil moisture content

ABSTRACT

Accelerated climate warming is causing significant reductions in the volume of Arctic glaciers, such that previously ice-capped bare ground is uncovered, harboring soil development. Monitoring the thermal and hydrologic characteristics of soils, which strongly affect microbial activity, is important to understand the evolution of emerging terrestrial landscapes. We instrumented two sites on the forefield of a retreating Svalbard glacier, representing sediment ages of approximately 5 and 60 years since exposure. Our instrumentation included an ERT array complemented by adjacent point sensor measurements of subsurface temperature and water content. Sediments were sampled at each location and at two more additional sites (120 and 2000 years old) along a chronosequence aligned with the direction of glacial retreat. Analysis suggests older sediments have a lower bulk density and contain fewer large minerals, which we interpret to be indicative of sediment reworking over time. Two months of monitoring data recorded during summer 2021 indicate that the 60-year-old sediments are stratified showing more spatially consistent changes in electrical resistivity, whereas the younger sediments show a more irregular structure, with consequences on heat and moisture conductivity. Furthermore, our sensors reveal that young sediments have a higher moisture content, but a lower moisture content variability.

1 | Introduction

Arctic regions are warming at a rate of three to four times faster than the global average [1–2]. The Svalbard Archipelago, situated between 77° and 80° N, is one of the largest ice-covered terrestrial areas in the Northern Hemisphere outside of Greenland, with around 38,871 km² of ice-covered land at its neoglacial maximum. However, the extent of ice cover on the Svalbard

Archipelago is currently decreasing rapidly and has declined by 13% relative to its neoglacial maximum [3] due to anthropogenic warming.

The retreat of glaciers has exposed terrestrial landscapes comprising morainic sediments and readily destabilized diamictos susceptible to processes of reworking and redistribution [4–5]. Newly exposed glacier forefields can exhibit

This is an open access article under the terms of the [Creative Commons Attribution](https://creativecommons.org/licenses/by/4.0/) License, which permits use, distribution and reproduction in any medium, provided the original work is properly cited.

  2024 The Authors. *Permafrost and Periglacial Processes* published by John Wiley & Sons Ltd.

successional changes as a function of time. As such, a chronosequence approach can be used to characterize the development of soils with increasing sediment ages as a function of distance to the glacier snout [6–8]. The till covered landscapes emerging from beneath the retreating ice are rapidly colonized by microorganisms during the initial stages of the soil formation [9–10] and are sensitive to further climatological changes [11]. Deeper layers of the soil undergo successional changes more slowly than surface layers [12] and are likely to be carbon limited due to a lack of photosynthetically derived organic carbon [13], and thus, deeper layers may be less sensitive to changes in key drivers of microbial activity such as moisture and temperature. Conversely, deeper soil may contain old carbon that is thawing following glacial retreat, potentially stimulating microbial activity. The biogeochemical processes occurring in deglaciated sediments therefore drive early stages of soil formation and impact the wider Arctic environment including adjacent ecosystems. Yet, the rates of those biogeochemical processes depend on temperature and available moisture, which have not been well characterized in these sediments, neither at depth nor across time scales of weeks to months, seasonally, and over the timescale of pedogenesis (i.e., decades).

Repeat surveying or sampling in the Arctic can be challenging due to harsh weather conditions (especially during winter months) and distance from population centers; thus, a remote, autonomous method of monitoring such environments is desirable. Automated sensor arrays have proven to be effective in monitoring remote and/or harsh environments, such as the deployment by Boike et al. [14] in Svalbard, capturing the interplay between snow depth and soil properties throughout extensive periods of monitoring [15–16]. Electrical geophysical methods provide a fast, cost-effective, and minimally invasive way of imaging soil moisture. These methods are known to be sensitive to lithology, soil texture, and water content—including phase and salinity (e.g., [17–19]). More specifically, electrical resistivity tomography (ERT) has an extensive track record of applications in the field [20], including polar environments where imaging and monitoring active layer freeze–thaw dynamics [21], thermohydrological dynamics [22], or the shape of the permafrost table [18, 23] have all been undertaken. Traditionally used only for single one-off surveys or few repeat measurements, recent advancements in ERT technology have led to the emergence of automated monitoring devices, such as the PROactive Infrastructure Monitoring and Evaluation (PRIME) system. PRIME technology has been used successfully for monitoring near-surface hydrological processes in remote locations over many months [22, 24].

However, ERT does not directly measure soil physical properties, with parameters such as soil moisture and soil salinity being inferred from absolute or relative values of electrical resistivity. In order to make such inferences, complementary measurements or laboratory calibrations are often required [25–26]. Thus, point sensors have been used in conjunction with ERT for the study of soil water dynamics [27]. Another complementary method that can be used to ground truth ERT measurements is nuclear magnetic resonance (NMR), which provides direct measurements of liquid phase water in the subsurface [28]. Surface NMR (sNMR) methods are completely noninvasive and have been employed in permafrost and high

alpine scenarios on multiple occasions offering valuable information about the permafrost and active layer dynamics (e.g., [29–31]).

To better constrain our knowledge of how temperature and moisture dynamics vary with depth and over seasonal time scales in developing Arctic soil, we present results from a sensor installation in the forefield of the retreating Midtre Lovénbreen glacier, located on the island of Spitsbergen, Svalbard (Figure 1). The sensors consist of an ERT array able to capture soil electrical resistivity in 4D collocated with an in situ point sensor array capable of measuring soil temperature and water content. These variables were continuously monitored throughout the summer of 2021. We also report results from campaign-style sNMR measurements and laboratory analysis of sediment physicochemical properties. We specifically characterize electrical resistivity changes at two sites of different sediment ages (following glacier retreat) in order to better understand the hydrothermal mechanisms shaping soil formation in the High Arctic. We describe sediment physical properties, focusing on sediment thermal gradients and sediment moisture availability during summer—as these factors are known to strongly influence sediment biological activity.

2 | Materials and Methods

2.1 | Study Site

Midtre Lovénbreen (ML) is a polythermal non-surge-type valley glacier [34] with a north-facing catchment located on the island of Spitsbergen, Svalbard Archipelago (Figure 1), approximately 5 km SE of Ny-Ålesund (78° 53' N, 11° 59' E). The extent of the moraine surrounding ML (Figure 1B) suggests it has receded at a rate of approximately 14 m per year [35] since its neoglacial maximum, which was likely to have been around 1890 according to photographic records [36]. The retreat of the glacier has left behind complexes of moraine mounds, braided outwash, lakes, and linear trains of supraglacial debris and a chronosequence of sediments with the oldest sediments closer to the neoglacial maximum line and the youngest sediments closest to the glacier snout. Such chronosequences constitute suitable environments for studying the processes of soil formation [8]. The dominant lithological rock units in the ML glacier catchment are a conglomeration of primarily felsic igneous fragments interspersed with metasediments including carbonate rocks and coal seams [37]. Between the edge of the moraine and the Kongsfjord shoreline, there are some established soils, made up of much older sediments (approximately 2000 years since glacier retreat; [38]) situated on top of Wordiekammen gypsum bedrock (Figure 1A). The West Spitsbergen Current warms the west coast of Spitsbergen Island generating a relatively mild climate for its latitude. According to Norwegian meteorological institute data (available at Seklima [39] web portal), Ny-Ålesund has experienced an increase in mean annual air temperature from -5.55°C between 1993 and 2002 to -2.51°C between 2013 and 2022. In terms of mean annual precipitation, these have not increased in the last 30 years with recorded values of around 420 mm.

We selected four sites along this chronosequence for sampling (SL 1–4 in Figure 1B) with ages of approximately 5–10, 60, 120, and 2000 years old, respectively [38], and installed a network of buried sensors at the youngest two sites, located closest to the

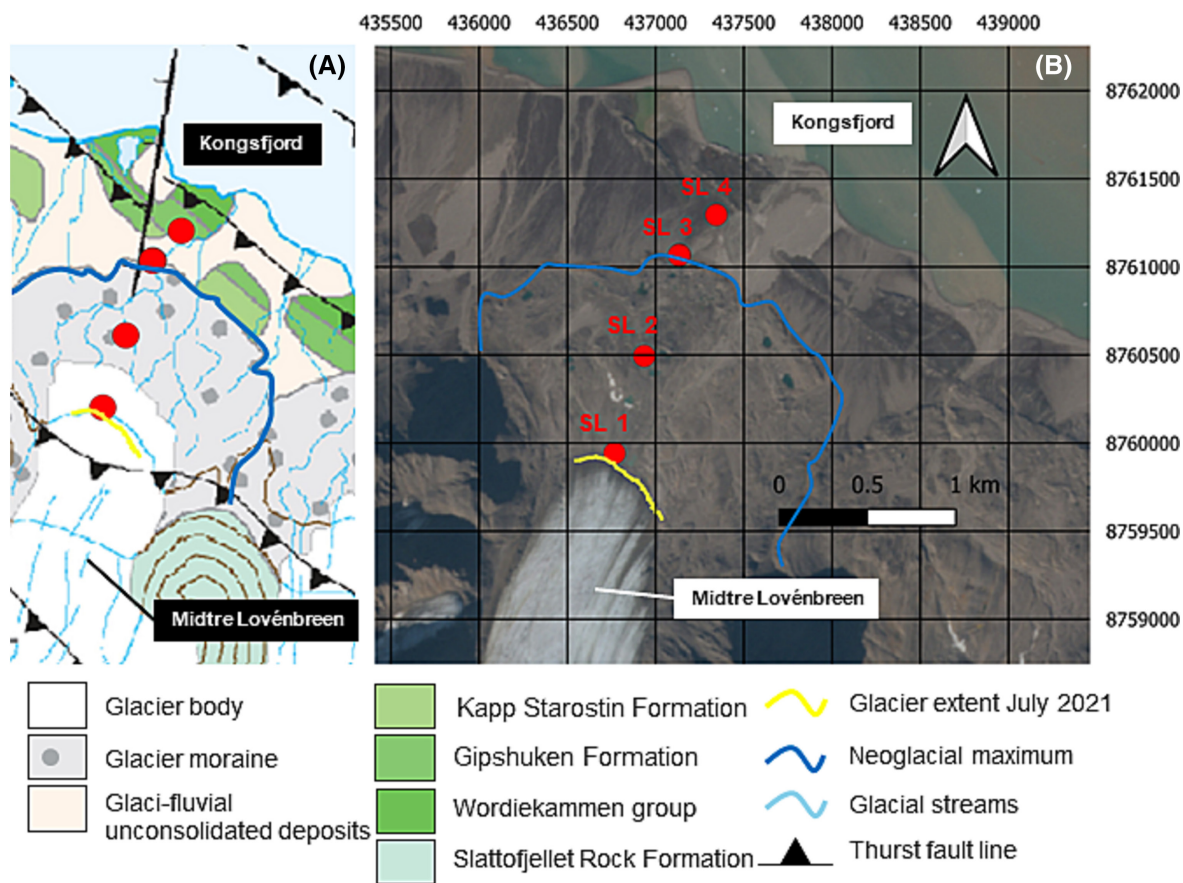


FIGURE 1 | Location of study site. (A) Svalbard archipelago with a blue dot indicating the location of the field site. (B) Geological map of Midtre Lovénbreen glacier forefield [32]; © Norwegian Polar Institute) with red dots indicating sediment sampling locations. (C) Satellite image from 2021 of Midtre Lovénbreen glacier forefield [33]; © Norwegian Polar Institute).

glacier snout (SL 1 and SL 2, ages of 5–10 and 60 years, respectively). SL 1 has a flat topography with the shallow subsurface comprising a mixture of predominantly silty sediments, gravel and boulders (0.10–1 m length), and a shallow water table (0.5 m depth) at the time of sensor installation (July 2021). The site is characterized by patches of moss and biological soil crusts and interspersed among the silty material in between large angular rocks. SL 2 is characterized by moraine hummocks and glacial stream bed features. Sensors were installed on a relatively flat moraine hummock, and the sediment was aggregated, with localized occurrences of lichens, biological soil crusts, and vascular plants such as *Salix polaris*, *Dryas octopetala*, and *Saxifraga oppositifolia*, which are common in the area [40], and dominate the forefield of the adjacent Austre Brøggerbreen glacier [41].

2.2 | Sediment Sampling and Characterization

Sediment was sampled from SL 1–4 in September 2020. From every location three bags of 100 g loose sediment and three cylindrical sediment cores (5 cm diameter × 2.5 cm height) were sampled from the top surface layer (0–25 cm). For the undisturbed samples, plastic PEEK cylinders were gently inserted into the ground's surface, using a hammer and a punch tool, and were extracted by careful removal of the surrounding material. All samples were wrapped in clingfilm for preservation and transported to the British Geological Survey labs in the United Kingdom for further analysis. Subsequent laboratory tests

aimed to identify the sediment's texture, porosity, pH, cation exchange capacity (CEC), and phosphorus content. Porosity was calculated as the percentage of the total sediment volume occupied by water at saturation. The sediment was then air-dried and sieved to under 2 mm. From this fraction, sediment particle size distribution was determined using a Beckman Coulter LS13 320 laser diffraction particle size analyzer. pH was measured with a GLpH meter using a mixture of sediment (150 g) and distilled water (75 mL). Phosphorus content was measured with an iCap 6500 Duo ICP-OES spectrometer. For total CEC determination, a small sample of sediment was washed with ammonium acetate, which displaces all other nutrient cations in the sediment, allowing the fraction of each cation in solution to be measured [42]. The undisturbed sediment cores were also scanned using X-ray computed tomography (CT) with a MSCL-RXCT scanner set at 130 kV, 450 μ A, 1 min scan time obtaining a 106 μ m resolution. In this experimental setting, the sample rotates, and the source–detector pair is fixed to allow projections from different angles. Subsequently, the raw X-ray scans are used to digitally reconstruct the sediment core volume, which can be further cross-sectioned to allow an in-depth spatial interpretation.

2.3 | Surface Nuclear Magnetic Resonance (sNMR)

Surface nuclear magnetic resonance (sNMR) is used to directly measure liquid phase water in the subsurface [28]. An sNMR

sounding uses a wire loop to generate a transient electromagnetic pulse in order to elevate hydrogen nuclei into an excited state, followed by a secondary field generated from the relaxation of the same atoms into their equilibrium. The secondary response provides information about the quantity and distribution of water in the subsurface. The amplitude of the secondary field is related to groundwater quantity, distinguishing between bound and free fractions, while the rates of decay of the field are related to pore size distribution and availability of groundwater [43].

Two snapshot sNMR surveys were conducted during July 2021 at SL 1 and SL 2 (Figure 1C). An MRS-MIDI II device was used operating with a 10-m square loop, which measured the free induction decay (FID) of the signal. The MRS-MIDI II is a relatively low power instrument capable of transmitting about 30 A of current. The corresponding depth of investigation (depth below acquired data is no longer sensitive to physical properties of the ground) is about 6–7 m. Estimates of the relaxation times characteristic of FID decays are obtained by fitting a sum of exponentially decaying sinusoids to the secondary voltage for all pulse moment measurements in the sounding. Sixty-four stacks of each pulse moment were collected. Noise levels after signal averaging were in the 2–3 nV range - exceptionally low for sNMR measurements.

2.4 | Point Sensor Installation

In proximity (within 5 m) of SL 1 and SL 2, the field sites were instrumented with point sensors. At both locations, 24 Teros-11 sensors were implanted into the wall of four 1-m-deep boreholes (six per borehole); these measure soil temperature, soil volumetric water content, and soil electrical resistivity. The boreholes were not lined and were refilled with the material extracted during drilling. A snow depth sensor was fixed approximately 2 m above the surface of the boreholes (Figure 2A, right). All sensors are connected to a Campbell Scientific CR1000X logger

recording hourly data for each measured parameter. The system is powered from a 250 Ah battery bank sustained by a 10 W solar panel.

2.5 | Electrical Resistivity Tomography

2.5.1 | Deployment and Data Acquisition

On each site, a PRIME system was deployed. PRIME is an automated, low power, multi-channel instrument that makes continuous measurements of soil electrical resistivity. This allows uninterrupted monitoring of the sites as 4D electrical resistivity tomography (ERT) datasets are recorded [24]. The system is powered from a battery bank (three lead acid batteries of 105 Ah each), sustained by a 110 W solar panel and a 300 W wind turbine (Figure 2B). Any excess power obtained from either the solar panel or the wind turbine is redirected and used as heat inside the system's waterproof container. PRIME utilizes six lines of 37 (222 in total) tubular electrodes placed 30 cm apart (inter-row and inter-electrode) and trenched into the top 20 cm of the ground (Figure 2A, left). One complete dataset is acquired every 2 days, containing 3696 normal measurements of soil apparent electrical resistance (R_n). For each individual measurement, a four-electrode dipole-dipole configuration is automatically selected, with two potential and two current electrodes, respectively. The geometric factor corresponding to each specific electrode configuration is taken into account in order to calculate electrical resistivity. An additional 3696 reciprocal measurements (R_r) accompany every dataset, where the current and potential electrode pairs are switched [44], bringing the total measurement time to 2 h and 8 min. During acquisition, measurements are also stacked for quality assurance.

The SL 1 electrode array has a N–S orientation, with one end (S) closer to the glacier snout. SL 2 electrode array has a NW–SE orientation, with one end (SE) closer to moraine hummock features and the other end (NW) closer to a moraine stream channel.

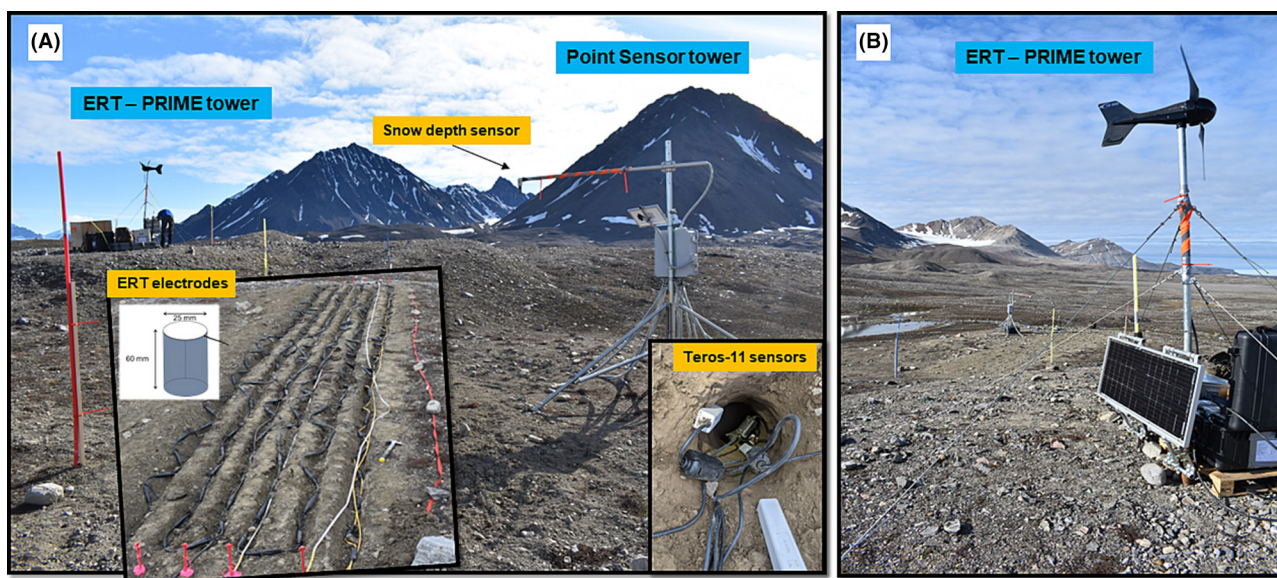


FIGURE 2 | Sensor installations in SL 2. (A) Sensor towers and PRIME electrode array. (B) Tower structure supporting the PRIME's wind turbine and solar panel in the foreground.

2.5.2 | Data Processing

Every dataset was filtered to remove negative apparent resistivities, and reciprocal errors greater than 5% and the apparent resistivity pseudo sections were checked for outliers. The reciprocal error (E_r) was defined as

$$E_r = \frac{100(R_n - R_r)}{R_m}, \quad (1)$$

where R_m is the mean value between R_n and R_r . Data quality was excellent in this case with more than 95% retained for all datasets.

In order to obtain a tomographic model of electrical resistivity, an inversion algorithm was used, in which a starting resistivity model is iteratively adjusted to achieve the best fit with the measured apparent resistivity values. In this case, 4D inversion was performed using Res3DInvX64 [45], which included all datasets from a 2-month period. For the purpose of discussion, a single suite of measurements (i.e., a dipole–dipole survey on a given day) is referred to as a time step. Each time step had a quadratic polynomial error model fitted (more details on how the error models are constructed in [46]) based only on the data from that time step, so data from less reliable steps were down-weighted. Given that all datasets had excellent data retention, the weights were very similar between time steps. For each data point, the data error estimated from the error model was combined with an estimate of the forward modelling error (taken to be 2%) using Gaussian error propagation. The inversion constraints were an L2 spatial constraint and an L1 temporal constraint (to allow for sharp changes in time, such as surface freezing). The spatial smoothing was isotropic with the same smoothness weightings in all Cartesian directions. The result is a time-lapse series of 3D resistivity tomograms, one corresponding to each of the two sites, with inversion misfits (absolute rather than root mean square as an L1 data constraint was used) of 1.87% for SL 1 and 2.77% for SL 2 (only one misfit value as there is only one 4D inversion per site). Finally, the resulting datasets were temperature corrected in order to isolate the effect of moisture content on the sediment's resistivity, acknowledging the rule

that resistivity above 0 °C decreases by 2% per °C increase in temperature [47]. We did not record temperatures below 0 °C over the course of the results window presented in this work. The temperature information used for calibration was the point sensor temperature data (Section 3.4), with data obtained at different depths used to calibrate different parts of the ERT model. Percentage electrical resistivity change was computed for every individual time step (TS) in reference to the first TS.

The time series of 3D models obtained through inversion was further spatially interpreted by dividing the model volume into separate zones, either lengthwise into five equally spaced regions, R1–R5, or vertically into three equally spaced layers, L1–L3. Through this analysis, lateral versus depth spatial trends can be made more apparent. Visual representation of the model can be found in the Figure S1. For the whole ERT model volume, but also for every one of the above zones, the change in the average electrical resistivity over time was obtained by computing the ratio between the average resistivity corresponding to every TS and the average resistivity of the first TS (referred to as ratio resistivity).

Figure 3 brings together all methods used in this work and their corresponding datasets. ER tomograms greatly benefit from adjacent measurements, firstly by spatially contextualizing the sites through soil physicochemical parameters and VWC distribution with depth and secondly by utilizing a continuous calibration over time using soil temperature and VWC point sensor datasets. This approach improves our understanding of the soil's hydrological regime with consequences for the establishment of microbiological activity and overall ecosystem evolution.

3 | Results

3.1 | Sediment Properties

We detected differences in sediment physicochemical properties between sites. We found that the sediments closer to the glacier (SL 1) are alkaline and have a low CEC and a loam texture. X-ray CT scans reveal the presence of larger vesicles close to the top of the sample and of larger minerals (appear brighter due to

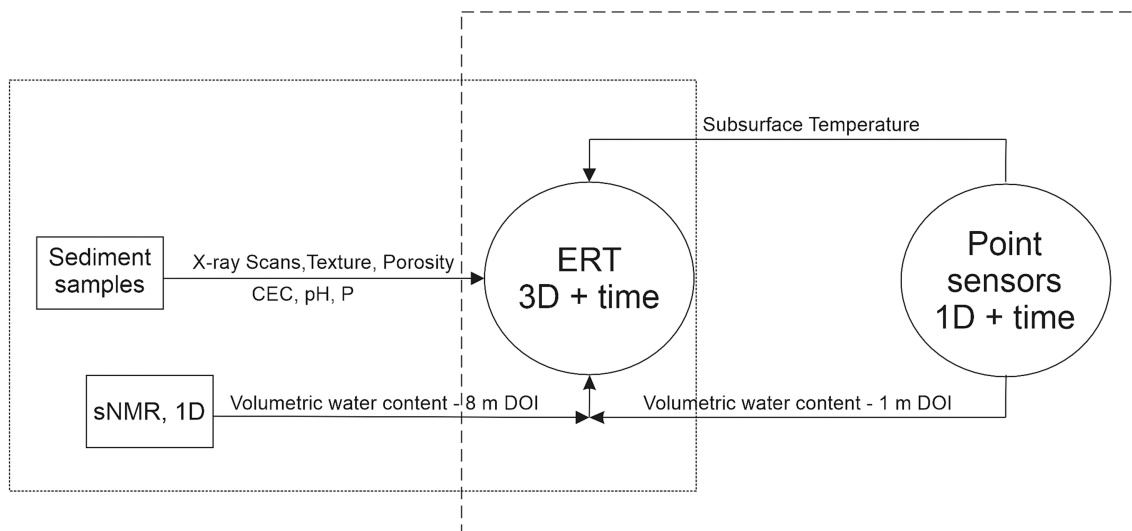


FIGURE 3 | Summary diagram of all methods and associated datasets analyzed. Solid squares indicate one-off datasets. Circles indicate automated time-lapse datasets. Dotted square groups together data that spatially characterize the sites. Dashed square groups data that temporally characterize the sites.

higher density) (Figure 4A1,A2). With increasing distance from the glacier (and thus sediment age), we found that the color and texture of the sediments changes (Figure 4A3,B3, Table 1); SL 2 sediments have a decreasing amount of silt, but more sand. The structure also appears to change, with older sediments showing a higher porosity, consistent with the change in texture. At SL 1, higher density material, such as stones, occupies approximately 25% of the sample volume. Distinctively, the sediment core at SL 2 appears to have a more cohesive structure on the CT scan, with fewer air pockets and minerals present (Figure 4B1,B2). At SL 3, the sediments' texture appears to be dominated by silt, with a large reduction in the clay and sand component. Sediments do not appear to change their capacity to hold positive ions and their acidity throughout the moraine, with CEC and pH being fairly similar between samples. Outside the moraine complex, samples from SL 4, had higher silt content, porosity, CEC, phosphorus content, and a lower pH.

3.2 | sNMR

sNMR surveys detected the presence of liquid water in the subsurface at both sites, with a peak in total water content present around the 1.5–1.8 m depth mark ($0.06\text{m}^3/\text{m}^3$ at SL 1 and

$0.045\text{m}^3/\text{m}^3$ at SL 2) (Figure 5A,B). SL 1 appears to have more total water than SL 2, this being confirmed by a shallow water table observed during borehole excavation at SL 1. However, SL 2 shows slightly more bound water close to the surface. Below 2 m depth, liquid water content reduces significantly at both sites, followed by another increase below 4 m only observable at SL 1. Due to instrumentation limitations, the sNMR struggles to detect water in very small pores, which explains the discrepancy between field and laboratory porosity values. Even though sNMR depth of investigation is higher than the other methods employed, we believe this information is essential to contextualize the description of our sites.

3.3 | Point Sensor and Weather Data

Teros-11 sensors recorded continuously from the beginning of August until the end of September 2021 (Figures 6A,B and 7A,B). There was no snow cover at our sites within the timeframe of our measurements. Mean daily air temperature fluctuated between -0.3 and 14°C and followed a general downward trend with localized exceptions during precipitation events (PE) when an increase is evident, with the largest event (PE 4) taking place between September 15 and 27 (Figures 6C and 7C).

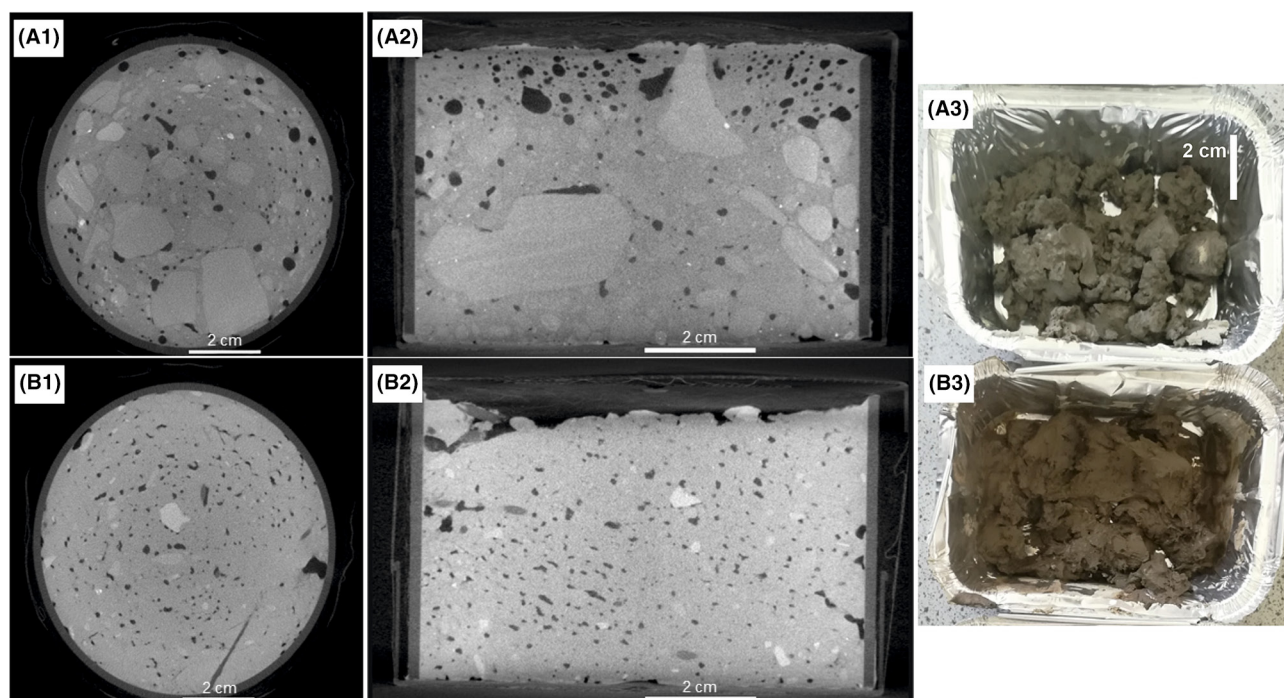


FIGURE 4 | CT images of the undisturbed sediment core volumes reconstructed post X-ray scanning. (A1) Horizontal and (A2) vertical cross sections through one of the cores from SL 1. (A3) Air-dried SL1 sample prepared for laboratory analysis. (B1) Horizontal and (B2) vertical cross sections through one of the cores from SL 2. (B3) Air-dried SL 2 sample prepared for laboratory analysis.

TABLE 1 | Sediment physicochemical properties corresponding to all sampling locations.

Sampling location no.	Approximate age (years)	Clay (%)	Silt (%)	Sand (%)	Porosity (%)	CEC (meq/100 g)	pH	Phosphorus (mg/kg)
SL 1	5–10	24.23 ± 1.57	40.56 ± 4.77	35.18 ± 3.30	13.5	2.6	8.78	527
SL 2	60	22.72 ± 1.36	25.59 ± 2.49	51.66 ± 1.68	19.6	4.7	8.45	641
SL 3	120	6.61 ± 0.52	68.53 ± 3.10	24.83 ± 2.62	—	1.7	8.83	241
SL 4	2000	4.79 ± 0.43	70.26 ± 3.24	25.03 ± 2.90	30.97	17.5	7.36	505

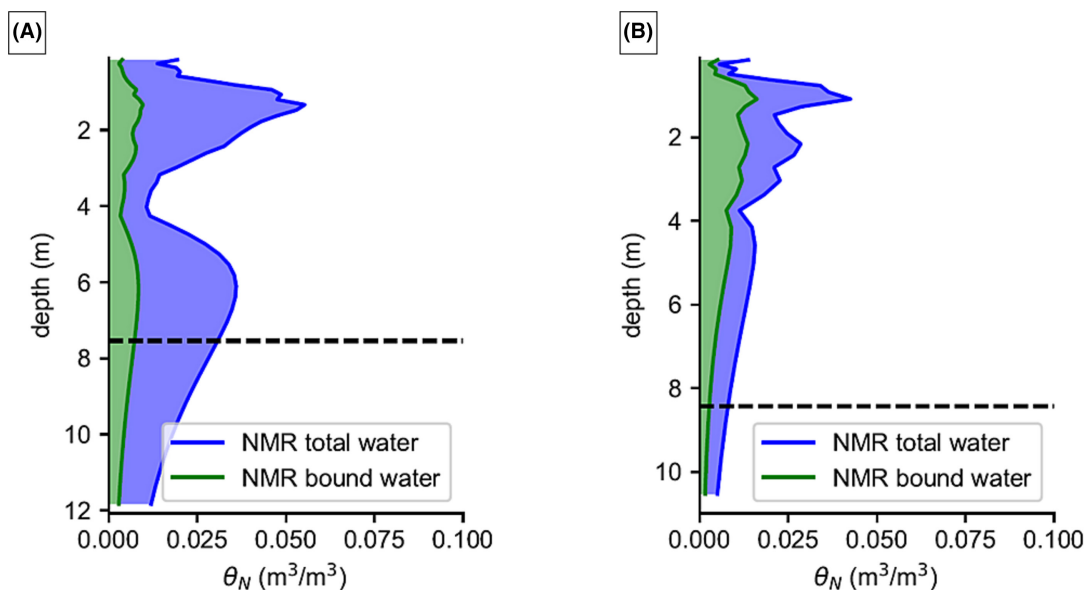


FIGURE 5 | sNMR results showing Water Content (θ_N) distribution with depth for (A) SL 1 and (B) SL 2. Dashed lines represent depth of investigation.

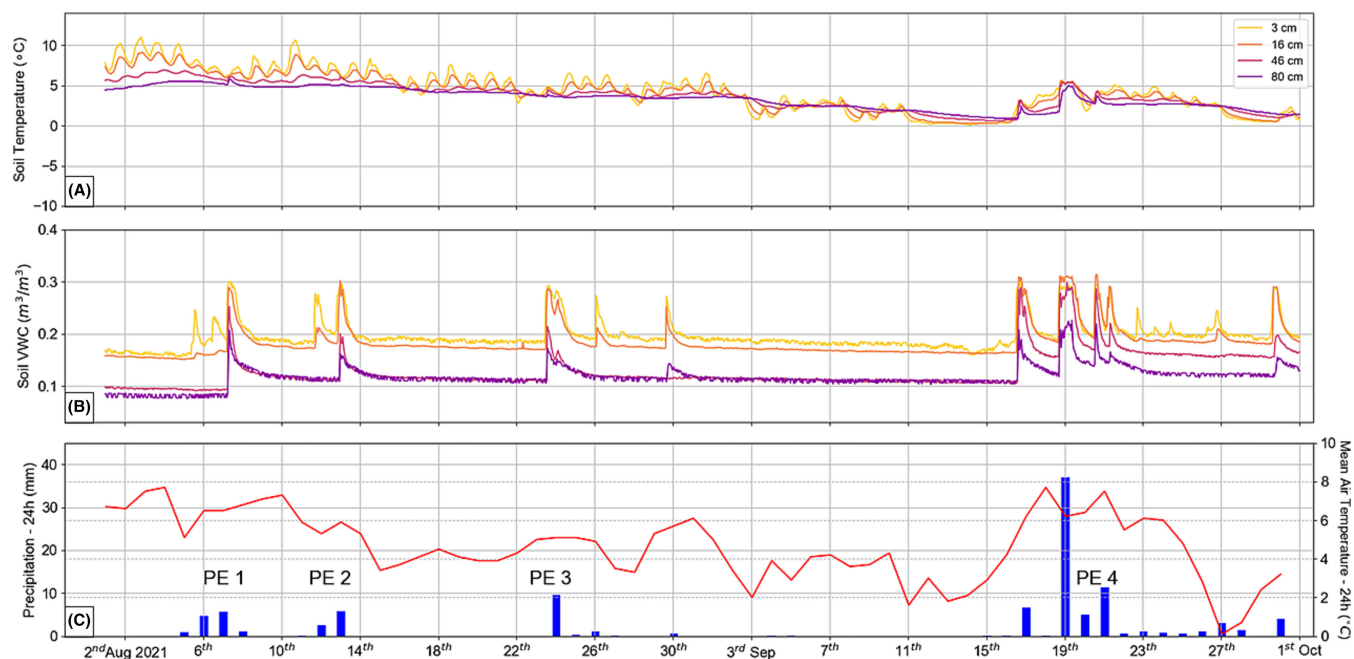


FIGURE 6 | Teros-11 point sensor data of (A) sediment temperature and (B) sediment volumetric water content (VWC) and weather records (available from [39]; the Norwegian Meteorological Institute/MET Norway, weather station in Ny-Ålesund) for the corresponding period of (C) precipitation and mean air temperature at SL 1. Occurrence of precipitation events (PE) is indicated. The inset in (A) indicates the depth (below the ground surface) of each sensor reading.

Sediment temperature data follow a similar trend at both sites, reflecting the increases in temperature during PEs. In addition, shallower sensors capture daily fluctuations in temperature, with slightly lower amplitudes at SL 1. SL 2 appears to be warmer than SL 1 when records begin and to have a steeper temperature gradient throughout the Arctic summer. SL 2 shows bigger differences between temperatures recorded at different depths, especially during dry periods. Both sites show higher temperatures in shallow than deeper layers throughout August, with the temperature difference reducing as air temperature decreases, and even dropping below deeper layer temperatures from the beginning of September.

Precipitation events (PE 1–4 on August 7, 13, and 25 and September 15, respectively) are reflected in the sediment volumetric water content (VWC) data by a sharp increase followed by a gently decreasing curve as the sediments dried. During the smaller PE in August, the increase in VWC was greater at SL 1. At SL 2, shallow depths are sensitive to all PE, whereas deeper depths at SL 2 are only sensitive to high-intensity PE (September 19). A change in VWC at SL 1 was apparent at all depths during all PEs. After the large precipitation event in September, for SL 1, the sensors indicate a return to the pre-event VWC levels, whereas for SL 2, they indicate an equilibrium around a higher VWC level post-event.

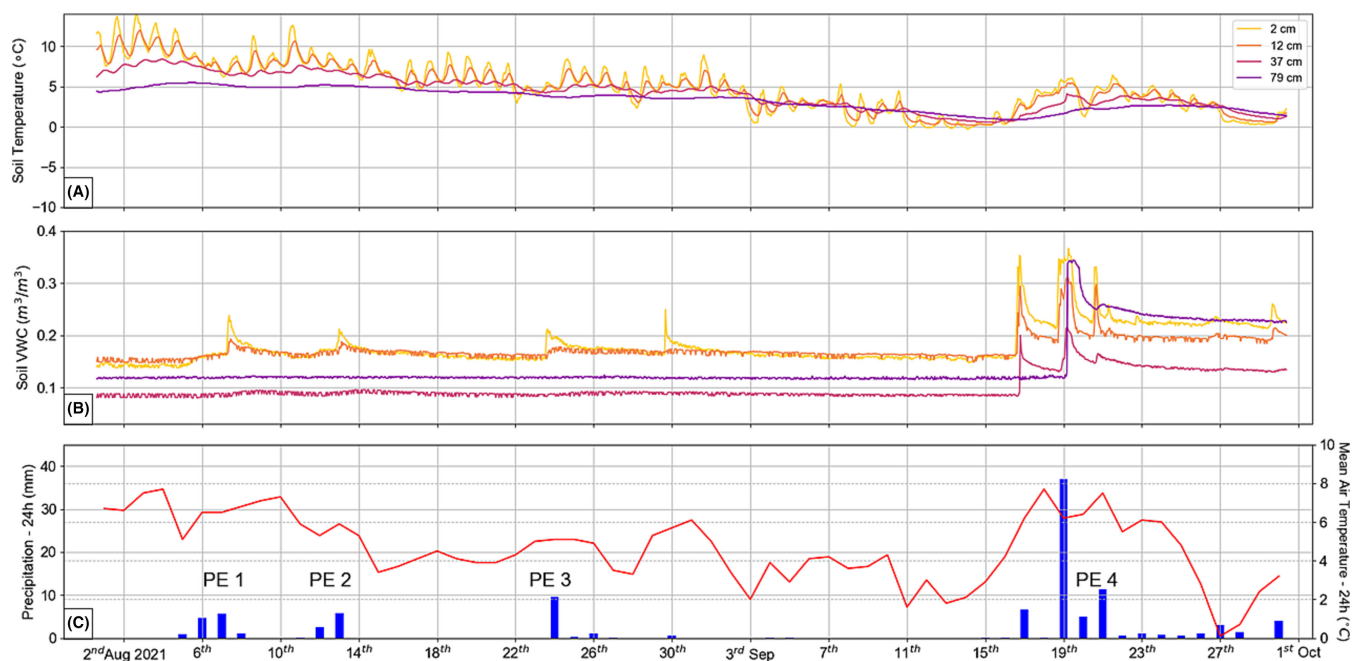


FIGURE 7 | Teros-11 point sensor data of (A) sediment temperature and (B) sediment volumetric water content (VWC) and weather records (available from [39]; the Norwegian Meteorological Institute/MET Norway, weather station in Ny-Ålesund) for the corresponding period of (C) precipitation and mean air temperature at SL 2. Occurrence of precipitation events (PE) is indicated. The inset in (A) indicates the depth (below the ground surface) of each sensor reading.

3.4 | Time-Lapse ERT

The SL 1 PRIME array recorded 30 complete datasets (August 2 to October 1, 2021) corresponding to time-steps (TS) every other day. For SL 2, we recorded 27 complete datasets due to instrumentation issues affecting August 6, September 13, and September 15, 2021.

We found that sediment electrical resistivity is generally higher at SL 2 than SL 1, with a low-resistivity zone ($<100 \Omega \cdot \text{m}$) at SL 1 near the glacier snout (Figure 8, TS 0). The SL 2 ERT model exhibits a well-defined continuous surface layer (200–500 $\Omega \cdot \text{m}$) extending to approximately 30 cm beneath the ground surface (Figure 9, TS 0) overlying a more resistive layer ($>1000 \Omega \cdot \text{m}$) (30–100 cm). We are only showing ERT data down to 1 m depth in order to match the depth attained by the point sensor installation.

Time-lapse ERT captured the percentage change in electrical resistivity over time, where areas of positive percentage change indicate that the site has become drier and areas of negative change indicate an increase in sediment moisture content. Our instrumentation captured the changes in resistivity following precipitation events at both sites (we present selected time steps in order to reflect such changes in Figures 8A and 9A). The succession shown here of TS 21–TS 24 (SL 1) and TS 20–TS 21 (SL 2) shows a drop in resistivity, which coincides with the largest precipitation event recorded. However, on the glacier side of the SL 1 model, we did not detect a drop in resistivity during the precipitation event.

Dividing the ERT imaged volume ($10.8 \times 1.5 \times 1 \text{ m}^3$) into different zones (Figure S1) allows a more in-depth investigation of spatial variability of resistivity. When looking at different regions of the ERT volume (Figures 8B and 9B), it can be observed that SL 2

shows a more homogeneous change over time than SL 1. SL 2 displays a general tendency of increasing in electrical resistivity (values over 1 in Figure 9B) as opposed to SL 1, which shows long periods where the regions are less resistive than the values at TS 0 (Figure 8B). Precipitation events are also evident here by sudden drops in ratio values. Furthermore, ER throughout SL 2 seems to stabilize at lower values after PE 4 than the ones recorded right before the start of PE 4. When the ERT volume is divided by depth (Figures 8C and 9C), we observe a similar tendency for an increase in resistivity for SL 2. The shallowest layer at SL 1 appears not to incur a negative change in resistivity as large as deeper layers do during PE 4 and shows a rebound in resistivity post the event. On the other hand, in SL 2, all layers reduce their resistivity (by 20%–40%) during PE 4 and subsequently show an increase after the event (10%–15%), but not up to the pre-PE 4 levels.

4 | Discussion

4.1 | Soil Formation

Soil formation is dependent on a variety of factors, such as climate, organic matter, relief, parent material, and time, with each combination of determinants generating different soil properties and profile characteristics. Parent material is an important driver of soil formation and its physical and chemical characteristics [48]. Our data (Table 1 and Figure 4) show that sediments from a different geological setting (SL 4) exhibited very distinct physicochemical properties. If discussing only sediments sampled within the moraine complex, they all have glacial diamicton as a sedimentary basis [49]. However, it is worth noting that glacial diamicton can itself exhibit different grain size distributions across a glacier forefield. Sediments at SL 2, estimated

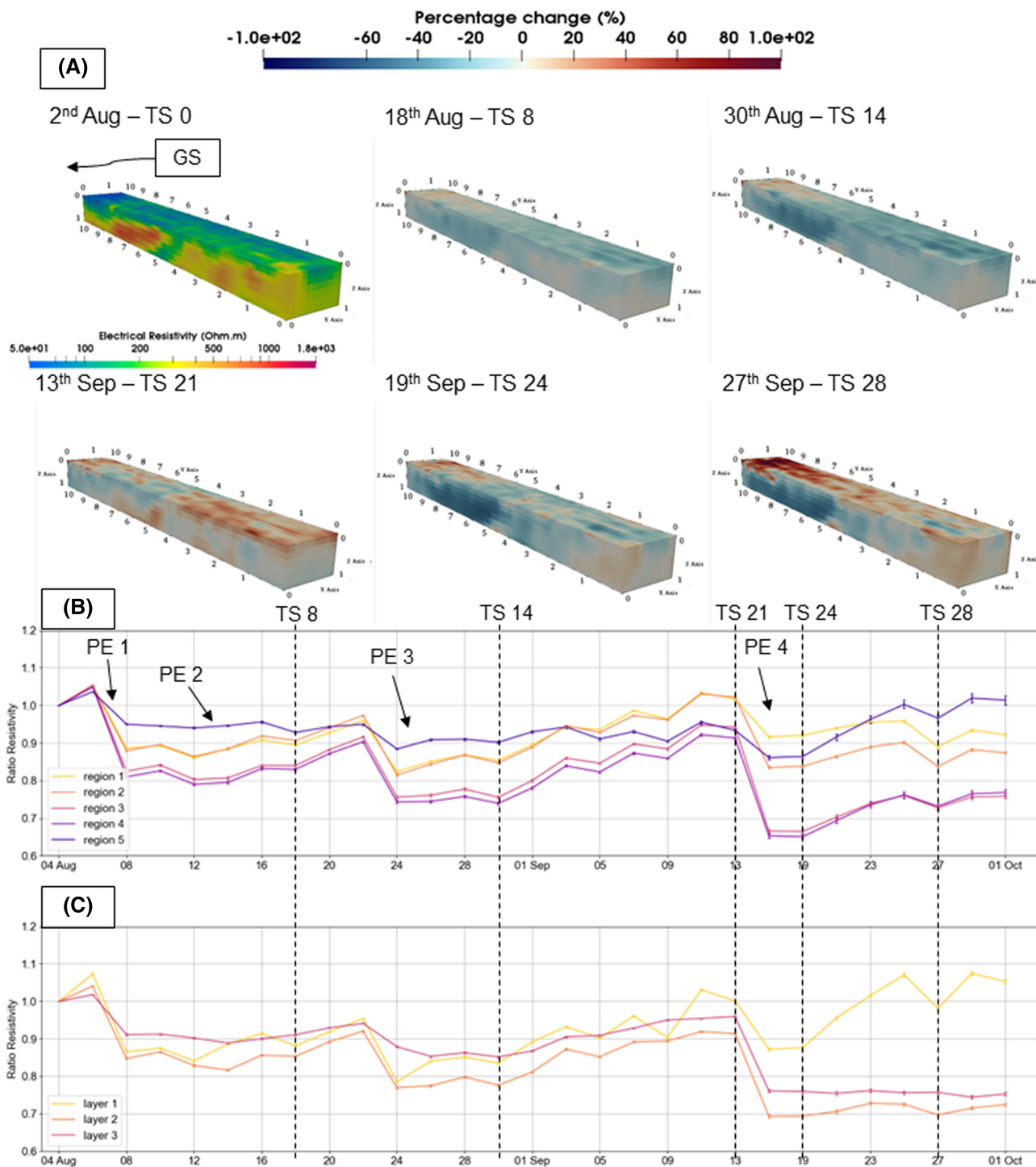


FIGURE 8 | (A) Six selected ERT time steps (TS), representing percentage resistivity change in reference to initial TS 0 (representing absolute values of electrical resistivity) corresponding to SL 1 (August–October 2021). GS (glacier side) indicates that ML glacier is nearer to that side of the model. (B) The change of average electrical resistivity over time corresponding to (B1) different regions and (B2) different layers of the ERT model. Occurrence of precipitation events (PE) is indicated. Dotted lines correspond to the ERT time steps in (A).

to be around 60 years old, show signs of prolonged erosion and weathering, with the amount of time exposed to physical weathering processes (including precipitation, melt water stream flow, or freeze–thaw) impacting the inherent properties. Sediments at the older site (SL 2) have an internal structure consisting of fewer vesicles and smaller minerals, when compared to the younger site (SL 1), a sign of constant alteration over time, that allowed the escape of gas and the erosion of minerals. Older

samples (SL 3 and SL 4) are also texturally different, with a lower clay proportion, which can be explained by clay migration in sediments such as these, with a low exchange capacity [50]. Sediments in SL 4, outside of the moraine complex, are likely to have a different origin by isostatic heaving processes due to their proximity to the shoreline. In a similar study, looking at soil properties along a glacier sediment chronosequence, Kabala and Zapart [51] found a reduction in clay fraction with

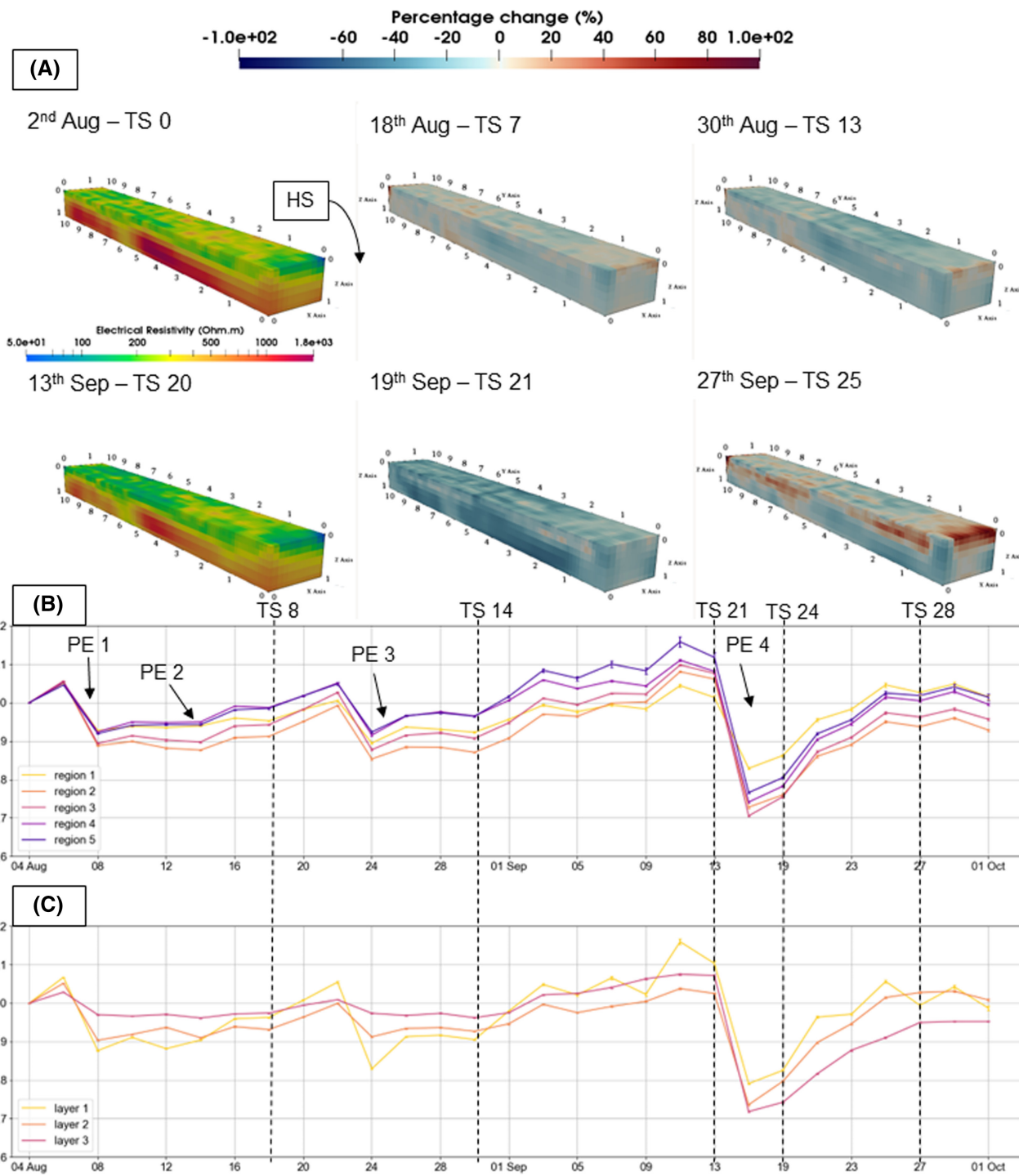


FIGURE 9 | (A) Six selected ERT time steps (TS), representing percentage resistivity change in reference to initial TS 0 (representing absolute values of electrical resistivity) corresponding to SL 2 (August–October 2021). HS (hummock side) indicates that moraine hummock features are nearer to that side of the model. (B) The change of average electrical resistivity over time corresponding to (B1) different regions and (B2) different layers of the ERT model. Occurrence of precipitation events (PE) is indicated. Dotted lines correspond to the ERT time steps in (A).

sediment age attributing it to a repeated washing-out of fine particles during spring melt water. On a proglacial area in the Swiss Alps, Mavris et al. [52] showed that chemical weathering and clay mineral transformation can occur right after glacier retreat, at an early stage of soil formation. Apart from the clay fraction, the silt–sand ratio of sediments dictates their susceptibility to frost heaves and cryoturbation [53]; therefore, siltier sediments such as the ones found at SL 3 and SL 4 can favor the formation of cryostructures.

The distance from the glacier, a consequence of the passage of time, has arguably a direct impact on the soil properties. Firstly, proximity to the glacier implies a different thermal regime; hence, a different sediment reaction to changes in air-temperature and influx of precipitation. Irvine-Fynn et al. [54] has linked thermoerosional processes with the reworking of the glacier forefield. Secondly, ML is a higher topographical unit than its forefield. Regions closer to the glacier snout would therefore benefit from a shelter against wind erosion but potentially

receive a higher input of liquid precipitation or melt water coming off the glacier slope. Glaciofluvial processes are likely to have contributed to sediment deposition and modelling of the glacier moraine, with older sediments (SL 2) experiencing a longer exposure time to environmental factors, such as melt water erosion. The relatively flat, unaltered topography of SL 1 would directly impact the site's drainage system. During the stages of soil formation, vegetation is set to appear given the right conditions. According to Kabala and Zapart [51], on their recently deglaciated study site in SW Spitsbergen, vegetation started to emerge 5–6 years after deglaciation. The low weathering intensity, including carbonate leaching, is assumed to be related to the slow succession of vegetation [55].

The timeframe we discuss here, 120 years of glacier retreat, is too short to expect a major transformation in chemical properties, even though there is clear evidence that chemical weathering is taking place [56]. Wietrzyk et al. [57] describes the accumulation of elements (e.g., total organic C, total N) due to weathering using nonlinear functions, a noticeable increase taking place after 50–60 years post deglaciation. This may emphasize that the data gathered from the two monitoring stations correspond to distinct stages of soil formation. Furthermore, the physicochemical characteristics discussed here establish a basis and a complementary framework for our sensor data interpretation, which will describe the thermal and hydrological regime of recently deglaciated sediments.

4.2 | Sediment Temperature and Water Content in Response to Precipitation Events

Point sensor data allow us to directly assess the sediments' response to changes in air temperature and precipitation. As pointed out in Section 3.3, SL 2 tends to be warmer than SL 1 and has a steeper temperature gradient throughout the sensor records. ML glacier, a large mass colder than the mean air temperature throughout the Arctic summer, slightly lowers the temperature of the sediments in their proximity and regulates their gradient in time and depth. Despite having 24 h of daylight until the 27th of August, on the ML forefield, point sensors picked up daily fluctuations in temperature. This is a consequence of local topography blocking direct sunlight, an effect more pronounced at SL 1 where the amplitude of such fluctuations was up to 2–3 °C higher than at SL 2 in early August 2021.

Even though all PEs were captured by sensors at both instrumented sites, there were differences in the magnitude of VWC levels detected during PE 1–3. Proximity to the glacier slope determined a higher precipitation influx at SL 1, and the presence of hummocks and stream beds at SL 2 determined a more enhanced drainage, causing less water to enter the sediment system. Szymański et al. [53] propose that soil wetness is the most important soil forming factor in proglacial areas. The amount of moisture will affect the depth and rate of freezing and thawing [58–59]. The VWC distribution therefore can be an indicator of the soil's stage of development, with an older soil that shows enhanced drainage thawing earlier and faster than a younger soil [58].

Deeper sediment layers (>30 cm) saw an increase in VWC at SL 1, whereas at SL 2 the VWC remained unchanged, simply because the influx of precipitation was not sufficient to overcome

potential evaporation for water to reach respective depths [60]. However, during PE 4, which saw the largest quantities of precipitation of the presented record, SL 2 VWC increased significantly at all monitored depths. The VWC levels post PE 4 were higher than before the event indicating water has been stored in the sediment pore network at SL 2. By contrast, VWC levels at SL 1 returned to pre-PE 4 levels after the event, indicating a lower water storage capacity than the SL 2 sediments, potentially determined by the difference in available porosity (see Table 1). This hypothesis agrees with He and Tang's [61] finding that bulk density decreases with sediment age on a proglacial chronosequence.

PEs also had a clear impact on sediment temperature at both sites. During PEs, daily fluctuations in temperature are attenuated greatly due to water acting as a thermal regulator. In addition, air temperature and consequently sediment temperature tended to rise during PEs due to the intense cloud coverage creating a greenhouse effect over the area. Boike et al. [14] report a 16-year record of soil water content measurements down to 1 m depth, monitored in the vicinity of Ny-Ålesund research village. During summer months, the records show similar near-surface VWC values and a similar increase in sediment temperature during PE.

4.3 | Continuous 3D ERT Monitoring and sNMR Measurements

A continuous record of 3D ER tomograms offers an opportunity to track soil water storage and movement over time and in space. Nonetheless, this dataset can be subjected to sources of error, which lead to misinterpretation of results. Among potential sources of measurement error, electrode positioning or poor ground-electrode contact are likely candidates in an Arctic, remote environment. We tried to minimize their effect by acquiring stacked and reciprocal measurements. Even though it is considered a minimally invasive method, ERT, through the electrode array installation, disturbed the site's surface and near subsurface to a certain degree. This can have an influence on small-scale hydrology. However, upon the inspection of the resulting images, we did not observe obvious preferential flow paths along the electrode lines.

sNMR detected more total liquid water close to the surface at SL 1, which was confirmed by direct observations while excavating the sensor boreholes. ERT models for SL 1 also capture a zone of low resistivity on the glacier side of the model. However, with a higher porosity and consequently larger pore surface area, SL 2 sediments hold slightly more bound water. The way the electrical resistivity profile changes over time is different between sites. SL 1 appears to have a smaller change overall before the large precipitation event, but a more pronounced positive change thereafter. This suggests that the hydraulic conductivity at SL 1 is lower than at SL 2. Electrical resistivity values are influenced by a variety of factors, namely, saturation, soil structure, clay content, and temperature [19]. Given that the ERT results have been temperature calibrated and the clay content is similar between sites, the low resistivity values are most likely indicative of a higher sediment moisture content, confirming once again the above observations. According to Bockheim et al. [62], one of

the main soil forming processes in polar areas is permanent or periodic water saturation of sediments, which can lead to sediment gleization, a reduction and removal of iron and manganese oxides from sediments. One indicator of gleyic sediments is their gray color, which we also observed on SL 1 samples (Figure 4A3). The apparent moisture abundant layer extends only to about 1.7 m depth at SL 1, followed by a steep drop in liquid water content. According to the literature, this could be explained by the presence of buried ice underneath a shallow layer of debris [4, 63]. This layer was unfortunately beyond reach given depths of investigation associated with our ERT electrode configuration. Deeper DC resistivity studies have been conducted in Svalbard [64–65], imaging a shallow active layer (<3 m) above the permafrost, with resistivity values in the range observed in our work (200–400 Ω .m). However, the resistivity value range depends on how much liquid moisture is available in the near subsurface at the time of imaging. For example, areas closer to the glacier snout at SL 1 recorded resistivity values of down to 50 Ω .m.

Overall, electrical resistivity values recorded at SL 2 were higher than at SL 1, despite the latter having large dense minerals in the sediment composition. As indicated by sNMR and point sensor data, SL 2 is generally warmer and drier, both contributing to higher values of electrical resistivity. At SL 1, the ERT results show us localized regions of higher resistivity, which are likely to be large boulders trapped in the glacier sediment. On the other hand, at SL 2, a well-defined more resistive layer with an upper boundary at 0.3 m depth is noticeable, which could be evidence of sediments being eroded, reworked and redeposited in time to form continuous layer boundaries. Furthermore, a two-layer system will dictate the way heat and moisture is conducted, the layer boundary acting as disruption to flow.

4.3.1 | ER Spatiotemporal Variability

Fluctuations in electrical resistivity over time are a result of net precipitation. SL 2 shows more areas of positive resistivity change right before PE 4 (Figure 8, TS 20) than SL 1 (Figure 9, TS 21), emphasizing the fact that due to its slightly different thermal and drainage regime, SL 2 dries faster, losing more moisture content than SL 1. Midgley et al. [63] point out that the Midtre Lovénbreen glaciofluvial drainage system is routed over ice-cored terrain, which results in high rates of thermo-erosion. Woo and Xia [66] argue that sediments in poorly drained sites, such as SL 1, are often rich in ice, retarding the development of a deep active layer. This would agree with the sNMR observation of a sharp decline in moisture content around 2.5 m depth, marking the boundary of a shallow active layer.

During PE 4, both sites displayed areas of high negative (up to 40% reduction) ER changes (Figure 8, TS 24; Figure 9, TS 21). The only exception was the less resistive region in SL 1 (previously discussed), potentially because it has already reached saturation, and thus, additional precipitation input would not change its moisture content. However, post PE 4, the same region displayed one of the strongest ER positive changes (up to 20% increase), with a lot of moisture contained in a shallow layer being more susceptible to evaporation. Generally, SL 1 showed stronger positive changes, indicative of loss of

moisture, than SL 2 post PE 4 (Figure 8, TS 28; Figure 9, TS 25); these are phenomena confirmed by point sensor data which indicate a quick return to pre-PE 4 values of VWC at SL 1. Szymański et al. [53] argue that proglacial sites with a moderate content of moisture are the most favorable for plant succession, as dry sites have water shortages and wet sites create anaerobic conditions and bolsters erosion. In this context, SL 1 appears to have too much moisture available, whereas SL 2, in addition to being exposed for a longer time, shows more moderate moisture fluctuations, which promoted localized plant growth.

Proglacial areas are characterized by a high variability of wetness, determined by a combination of factors, such as relief variability, sediment texture, and hydraulic properties of the exposed sediments [67–68]. Ratio resistivity change over time captured by ERT reflects such variability (Figures 8 and 9). The general tendency of SL 2 is to dry over time (ratio values greater than 1) (Figure 9B), whereas SL 1 appears to be wetter as records progress. This general behavior was previously explained by a thermal regime strongly influenced by a proximal glacier and an enhanced precipitation influx determined by the surrounding topography, as evidenced by point sensor measurements. Different regions of SL 2 seem to have a similar response to changes in VWC, indicating a certain degree of homogeneity and continuity of sediment layers, whereas SL 1 regions show an irregular response, an expected pattern from a young heterogeneous mix of sediments and gravel (Figure 8B). Post PE 4, SL 2 ratio change values seem to equilibrate at lower values than pre-PE 4 (5%–10% lower depending on layer), in agreement with point sensor measurements of VWC. However, values of ratio change corresponding to deeper layers of SL 1 remain low after PE 4, disagreeing with point sensor measurements that suggested a return to pre-PE 4 values of VWC. This could be explained by limited drainage at SL 1, a system with an undeveloped pore network, as suggested by CT scans and other sediment laboratory measurements (Section 4.1), and underlying buried ice or large boulders blocking water percolation at depth (ER Spatiotemporal Variability section). During a large rainfall event, the downslope movement will occur in the layer with higher hydraulic conductivity [69]; in this case, due to its texture and other observed physical parameters, SL 2 is prone to exhibit greater moisture movement.

The combination of methods employed in this study is essential to understand the physical and hydrological properties of the investigated site. For long-term monitoring of the shallow subsurface, continuous geoelectrical imaging in corroboration with point sensors can be used as a proxy for moisture content variability, a critical variable affecting microbial community development and activity [70]. Microbial communities in the ML forefield have been shown to change significantly during the first few decades of soil formation [11, 71, 72] and contribute to the build-up of soil organic matter [9, 71, 73].

Our instrumentation has the potential to reveal suitable hydrothermal conditions for microbial activity and growth in the developing forefield sediments. Continuous monitoring in combination with field sampling has the potential to determine when microbes in glacier forefield sediments might be most active, and also to explain the community heterogeneity in the context of the sediment hydrophysical properties.

5 | Conclusions

Monitoring the processes in recently deglaciated sediments is essential to better understand early-stage soil formation and how it is shaped by and impacts the wider Arctic environment. Here, we present physicochemical property analysis and a continuous measurement of ER, temperature, and VWC from a sediment chronosequence in the forefield of ML glacier in Svalbard, over the course of 2 months during the Arctic summer (August–September 2021). We found that sediments exhibit physical changes as they age, with greater porosity, but smaller minerals and less vesicles being associated with older sediments, characteristics that we attribute to erosion and sediment reworking over time.

Point measurements of VWC and continuous resistivity imaging showed higher moisture availability in sediments closer to the glacier snout due to the surrounding topography contributing to more water coming off the glacier slope and less drainage because of a relatively flat surrounding terrain. As a consequence of their location on the moraine and high levels of saturation, these younger sediments are shaped by gleization and a higher rate of thermoerosion. ERT monitoring of older sediments (at SL 2) revealed a well-defined layer stratification, corroborating our assumption that the glacial sediments were reworked and redeposited over time, transformed from an irregular mixture of clay, gravel, and boulders, which is present at SL 1. SL 2 also responded differently to temperature changes due to its increased distance from the glacier snout, appearing to be warmer and to respond faster to changes in air temperature. Moisture variability between sediment layers and their fast response to moisture influx suggest that these older sediments exhibit higher water flow. Finally, the older sediments showed a more spatially homogeneous change in ER potentially suggesting a more cohesive spatial development, whereas younger sediments showed a more heterogeneous change, which could imply that different areas will develop at different rates.

We conclude that continuous high-resolution geoelectrical monitoring has excellent potential to serve as a proxy for sediment hydrodynamics and thermal regime, offering important insights about the physical development of recently deglaciated sediments in time and space. This knowledge may be used to inform analyses of sediment microbiological activity for a better holistic understanding of soil evolution in the Arctic.

Acknowledgments

This work was funded by the NSF-UKRI Signals in the Soil program (award numbers, NERC: NE/T010967/1, NE/T010568/1; NSF: 1935651, 2015329, 1935689) and also received financial support from the NERC Covid Fund (administered by the British Antarctic Survey). This work also benefited from Trans-National Access support (project AMBER-ICE) from the European Union's Horizon 2020 project INTERACT, under grant agreement no. 730938. James Bradley also acknowledges support from the CNRS Chaires de Professeur Junior (CPJ).

We thank the UK Arctic Research Station and the Norwegian Polar Institute Sverdrup Station in Ny-Ålesund, Svalbard, as well as Svein Harald Sønderland, Juan Carlos Trejos, Justin Byington, Michael Jarzin Jr., Lara Vimercati, and Zhou Lyu for assistance and logistical support in the field.

Conflicts of Interest

The authors declare no conflicts of interest.

References

1. P. Chylek, C. Folland, J. D. Klett, et al., “Annual Mean Arctic Amplification 1970–2020: Observed and Simulated by CMIP6 Climate Models,” *Geophysical Research Letters* 49 (2022): 1–8, <https://doi.org/10.1029/2022gl099371>.
2. K. Isaksen, Ø. Nordli, B. Ivanov, et al., “Exceptional Warming over the Barents Area,” *Scientific Reports* 12, no. 1 (2022): 1–18, <https://doi.org/10.1038/s41598-022-13568-5>.
3. R. Martín-Moreno, F. Allende Álvarez, and J. O. Hagen, “‘Little Ice Age’ Glaciers Extent and Subsequent Retreat in Svalbard Archipelago,” *The Holocene* 27, no. 9 (2017): 1–12, <https://doi.org/10.1177/0959683617693904>.
4. T. D. L. Irvine-Fynn, N. E. Barrand, P. R. Porter, A. J. Hodson, and T. Murray, “Recent High Arctic Glacial Sediment Redistribution: A Process Perspective Using Airborne Lidar,” *Geomorphology* 125, no. 1 (2011): 27–39, <https://doi.org/10.1016/j.geomorph.2010.08.012>.
5. D. Mercier and D. Laffly, “Actual Paraglacial Progradation of the Coastal Zone in the Kongsfjorden Area, Western Spitsbergen (Svalbard),” in *Cryospheric Systems: Glaciers and Permafrost*, eds. C. Harris and J. Murton (London: Geological Society Special Publication, 2005), 111–117.
6. W. J. V. Vreeken, “Principal Kinds of Chronosequences and their Significance in Soil History,” *Journal of Soil Science* 26 (1975): 378–394.
7. L. R. Walker, D. A. Wardle, R. D. Bardgett, and B. D. Clarkson, “The Use of Chronosequences in Studies of Ecological Succession and Soil Development,” *Journal of Ecology* 98 (2010): 725–736.
8. R. Wojcik, J. Eichel, J. A. Bradley, and L. G. Benning, “How Allogenic Factors Affect Succession in Glacier Forefields,” *Earth-Science Reviews* 218 (2021): 103642, <https://doi.org/10.1016/j.earscirev.2021.103642>.
9. J. A. Bradley, J. S. Singarayer, and A. M. Anesio, “Microbial Community Dynamics in the Forefield of Glaciers,” *Proceedings of the Royal Society B* 281 (2014): 20140882, <https://doi.org/10.1098/rspb.2014.0882>.
10. S. K. Schmidt, S. C. Reed, D. R. Nemergut, et al., “The Earliest Stages of Ecosystem Succession in High-Elevation, Recently De-Glaciated Soils,” *Proceedings of the Royal Society B* 275 (2008): 2793–2802.
11. J. A. Bradley, A. M. Anesio, and S. Arndt, “Microbial and Biogeochemical Dynamics in Glacier Forefields Are Sensitive to Century-Scale Climate and Anthropogenic Change,” *Frontiers in Earth Science* 5 (2017): 26.
12. T. Rime, M. Hartmann, I. Brunner, F. Widmer, J. Zeyer, and B. Frey, “Vertical Distribution of the Soil Microbiota Along a Successional Gradient in a Glacier Forefield,” *Molecular Ecology* 24 (2015): 1091–1108.
13. K. R. Freeman, M. Y. Pescador, S. C. Reed, E. K. Costello, M. S. Robeson, and S. K. Schmidt, “Soil CO₂ Flux and Photoautotrophic Community Composition in High-Elevation, “Barren” Soils,” *Environmental Microbiology* 11 (2009): 674–686.
14. J. Boike, J. Nitzbon, K. Anders, et al., “A 16-Year Record (2002–2017) of Permafrost, Active-Layer, and Meteorological Conditions at the Samoylov Island Arctic Permafrost Research Site, Lena River Delta, Northern Siberia: An Opportunity to Validate Remote-Sensing Data and Land Surface, Snow, and Permafrost Models,” *Earth System Science Data* 11, no. 1 (2019): 261–299, <https://doi.org/10.5194/essd-11-261-2019>.
15. S. A. Malek, F. Avanzi, K. Brun-Laguna, et al., “Real-Time Alpine Measurement System Using Wireless Sensor Networks,” *Sensors (Switzerland)* 17, no. 11 (2017): 1–30, <https://doi.org/10.3390/s17112583>.
16. C. A. Oroza, Z. Zheng, S. D. Glaser, D. Tuia, and R. C. Bales, “Optimizing Embedded Sensor Network Design for Catchment-Scale Snow-Depth Estimation Using LiDAR and Machine Learning,” *Water Resources Research* 52, no. 10 (2016): 8174–8189.
17. C. Hauck, “Frozen Ground Monitoring Using DC Resistivity Tomography,” *Geophysical Research Letters* 29, no. 21 (2002): 12–1–12–4.

18. M. Kasprzak, "High-Resolution Electrical Resistivity Tomography Applied to Patterned Ground, Wedel Jarlsberg Land, South-West Spitsbergen," *Polar Research* 34, no. 1 (2015): 25678.
19. A. Samouëlian, I. Cousin, G. Richard, A. Tabbagh, and A. Bruand, "Electrical Resistivity Imaging for Detecting Soil Cracking at the Centimetric Scale," *Soil Science Society of America Journal* 67, no. 5 (2003): 1319–1326, <https://doi.org/10.2136/sssaj2003.1319>.
20. M. H. Loke, J. E. Chambers, D. F. Rucker, O. Kuras, and P. B. Wilkinson, "Recent Developments in the Direct-Current Geoelectrical Imaging Method," *Journal of Applied Geophysics* 95 (2013): 135–156.
21. M. Farzamian, G. Vieira, F. A. Monteiro Santos, et al., "Detailed Detection of Active Layer Freeze-Thaw Dynamics Using Quasi-Continuous Electrical Resistivity Tomography (Deception Island, Antarctica)," *The Cryosphere* 14, no. 3 (2020): 1105–1120, <https://doi.org/10.5194/tc-14-1105-2020>.
22. S. Uhlemann, B. Dafflon, J. Peterson, et al., "Geophysical Monitoring Shows that Spatial Heterogeneity in Thermohydrological Dynamics Reshapes a Transitional Permafrost System," *Geophysical Research Letters* 48, no. 6 (2021): 1–11, <https://doi.org/10.1029/2020GL091149>.
23. J. Doetsch, T. Ingeman-Nielsen, A. V. Christiansen, G. Fiandaca, E. Auken, and B. Elberling, "Direct Current (DC) Resistivity and Induced Polarization (IP) Monitoring of Active Layer Dynamics at High Temporal Resolution," *Cold Regions Science and Technology* 119 (2015): 16–28.
24. J. Holmes, J. Chambers, P. Wilkinson, et al., "Application of Petrophysical Relationships to Electrical Resistivity Models for Assessing the Stability of a Landslide in British Columbia, Canada," *Engineering Geology* 301, no. July 2021 (2022): 106613, <https://doi.org/10.1016/j.enggeo.2022.106613>.
25. G. E. Archie, "The Electrical Resistivity Log as an Aid in Determining Some Reservoir Characteristics," *Transactions of the American Institute of Mining, Metallurgical and Petroleum Engineers* 146 (1942): 54–62.
26. M. H. Waxman and L. J. M. Smits, "Electrical Conductivities in Oil-Bearing Shaly Sands," *Society of Petroleum Engineers Journal* 8 (1968): 107–122.
27. D. Michot, Y. Benderitter, A. Dorigny, B. Nicoullaud, D. King, and A. Tabbagh, "Spatial and Temporal Monitoring of Soil Water Content With an Irrigated Corn Crop Cover Using Surface Electrical Resistivity Tomography," *Water Resources Research* 39, no. 5 (2003), <https://doi.org/10.1029/2002wr001581>.
28. A. A. Behroozmand, K. Keating, and E. Auken, "A Review of the Principles and Applications of the NMR Technique for Near-Surface Characterization," *Surveys in Geophysics* 36, no. 1 (2015): 27–85.
29. T. P. Irons, K. E. Martin, C. A. Finn, B. R. Bloss, and R. J. Horton, "Using Nuclear Magnetic Resonance and Transient Electromagnetics to Characterize Water Distribution beneath an Ice Covered Volcanic Crater: The Case of Sherman Crater Mt. Baker, Washington," *Near Surface Geophysics* 12, no. 2 (2014): 285–296.
30. K. Keating, A. Binley, V. Bense, R. L. Van Dam, and H. H. Christiansen, "Combined Geophysical Measurements Provide Evidence for Unfrozen Water in Permafrost in the Adventdalen Valley in Svalbard," *Geophysical Research Letters* 45 (2018): 7606–7614, <https://doi.org/10.1029/2017GL076508>.
31. A. D. Parsekian, A. L. Creighton, B. M. Jones, and C. D. Arp, "Surface Nuclear Magnetic Resonance Observations of Permafrost Thaw Below Floating, Bedfast, and Transitional Ice Lakes," *Geophysics* 84, no. 3 (2019): N33–N45.
32. NPI, "Satelitt, Svalbard," accessed May 10, 2023a. https://geodata.npolar.no/arcgis/rest/services/Temadata/G_Geologi_Svalbard_Rasster/MapServer.
33. NPI, "Geologi, Svalbard," accessed May 10, 2023b. https://geodata.npolar.no/arcgis/rest/services/Basisdata/NP_Satellitt_Svalbard_WMETS_25833/MapServer.
34. M. J. Hambrey, M. R. Bennett, J. A. Dowdeswell, N. F. Glasser, and D. Huddart, "Debris Entrainment and Transfer in Polythermal Valley Glaciers," *Journal of Glaciology* 45, no. 149 (1999): 69–86.
35. M. J. Hambrey, T. Murray, N. F. Glasser, et al., "Structure and Changing Dynamics of a Polythermal Valley Glacier on a Centennial Timescale: Midtre Lovénbreen, Svalbard," *Journal of Geophysical Research: Earth Surface* 110 (2005): 1–19, <https://doi.org/10.1029/2004JF000128>.
36. A. Hamberg, "En resa till norra Ishafvet sommaren 1892," *Ymer* 14 (1894): 25–61.
37. W. Harland, L. M. Anderson, D. Manasrah, et al., *The Geology of Svalbard*, vol. 17, (Geological Society of London, Memoir, 1997).
38. I. D. Hodkinson, S. J. Coulson, and N. R. Webb, "Community Assembly Along Proglacial Chronosequences in the High Arctic: Vegetation and Soil Development in North-West Svalbard," *Journal of Ecology* 91, no. 4 (2003): 651–663, <https://doi.org/10.1046/j.1365-2745.2003.00786.x>.
39. Seklima, "Observations and Weather Statistics," accessed June 29, 2022. <https://seklima.met.no/>.
40. Å. Ø. Pedersen, P. Convey, K. K. Newsham, et al., "Five Decades of Terrestrial and Freshwater Research at Ny-Ålesund, Svalbard," *Polar Research* 41 (2022): 6310, <https://doi.org/10.33265/polar.v41.6310>.
41. H. Muraoka, H. Noda, M. Uchida, T. Ohtsuka, H. Koizumi, and T. Nakatsubo, "Photosynthetic Characteristics and Biomass Distribution of the Dominant Vascular Plant Species in a High Arctic Tundra Ecosystem, Ny-Ålesund, Svalbard: Implications for their Role in Ecosystem Carbon Gain," *Journal of Plant Research* 121 (2008): 137–145.
42. US EPA Method 9080, "Cation Exchange Capacity of Soils (Ammonium Acetate)," (1986).
43. A. C. Davis, N. Skibbe, and M. Müller-Petke, "First Measurements of Surface Nuclear Magnetic Resonance Signals in a Grounded Bipole," *Geophysical Research Letters* 46 (2019): 9620–9627, <https://doi.org/10.1029/2019GL084342>.
44. J. LaBrecque, M. Miletto, W. Daily, A. Ramirez, and E. Owen, "The Effects of Noise on Occam's Inversion of Resistivity Tomography Data," *Geophysics* 61 (1996): 538–548.
45. M. H. Loke, "RES3DINVx64 ver. 4.07 with multi-core and 64-bit support for Windows XP/Vista/7/8/10. Rapid 3-D Resistivity & IP inversion using the least-squares method," *Geoelectrical Imaging 2-D and 3-D. Geotomo Software*, (2017).
46. N. Lesparre, F. Nguyen, A. Kemna, et al., "A New Approach for Timelapse Data Weighting in Electrical Resistivity Tomography," *Geophysics* 82 (2017): E325–E333.
47. K. Hayley, L. R. Bentley, M. Gharibi, and M. Nightingale, "Low Temperature Dependence of Electrical Resistivity: Implications for Near Surface Geophysical Monitoring," *Geophysical Research Letters* 34 (2007): L18402.
48. R. Schaetzl and S. Anderson, *Soils: Genesis and Geomorphology* (Cambridge: Cambridge University Press, 2005), I–Vi.
49. M. J. Hambrey, D. Huddart, M. R. Bennett, and N. F. Glasser, "Genesis of "Hummocky Moraines" by Thrusting in Glacier Ice: Evidence From Svalbard and Britain," *Journal of the Geological Society* 154, no. 4 (1997): 623–632, <https://doi.org/10.1144/gsjgs.154.4.0623>.
50. C. McPhee, J. Reed, and I. Zubizarreta, "Core Sample Preparation," *Developments in Petroleum Science* 64 (2015): 135–179, <https://doi.org/10.1016/B978-0-444-63533-4.00004-4>.
51. C. Kabala and J. Zapart, "Initial Soil Development and Carbon Accumulation on Moraines of the Rapidly Retreating Werenskiöld Glacier,

- SW Spitsbergen, Svalbard Archipelago," *Geoderma* 175–176 (2012): 9–20, <https://doi.org/10.1016/j.geoderma.2012.01.025>.
52. C. Mavris, M. Plötze, A. Mirabella, D. Giaccai, G. Valboa, and M. Egli, "Clay Mineral Evolution Along a Soil Chronosequence in an Alpine Proglacial Area," *Geoderma* 165, no. 1 (2011): 106–117, <https://doi.org/10.1016/j.geoderma.2011.07.010>.
53. W. Szymański, M. Skiba, B. Wojtuń, and M. Drewnik, "Soil Properties, Micromorphology, and Mineralogy of Cryosols from Sorted and Unsorted Patterned Grounds in the Hornsund Area, SW Spitsbergen," *Geoderma* 253–254 (2015): 1–11, <https://doi.org/10.1016/j.geoderma.2015.03.029>.
54. T. D. L. Irvine-Fynn, B. J. Moorman, D. B. Sjogren, et al., "Cryological Processes Implied in Arctic Proglacial Stream Sediment Dynamics Using Principal Components Analysis and Regression," in *Cryospheric Systems: Glaciers and Permafrost*, eds. C. Harris and J. Murton (London: Geological Society Special Publication, 2005), 83–98.
55. S. M. Bernasconi and BigLink Consortium, "Weathering, Soil Formation and Initial Ecosystem Evolution on a Glacier Forefield: A Case Study From the Damma Glacier, Switzerland," *Mineralogical Magazine* 72 (2008): 19–22.
56. B. Velde and A. Meunier, *The Origin of Clay Minerals in Soils and Weathered Rocks* (Berlin-Heidelberg: Springer, 2008).
57. P. Wietrzyk, K. Rola, P. Osyczka, P. Nicia, W. Szymański, and M. Węgrzyn, "The Relationships Between Soil Chemical Properties and Vegetation Succession in the Aspect of Changes of Distance From the Glacier Forehead and Time Elapsed After Glacier Retreat in the Irenebreen Foreland (NW Svalbard)," *Plant and Soil* 428, no. 1–2 (2018): 195–211, <https://doi.org/10.1007/s11104-018-3660-3>.
58. J. V. Drew, J. C. F. Tedro, R. E. Shanks, and J. J. Korando, "Rate and Depth of Thaw in Arctic Soils," *Transactions of the American Geophysical Union* 39, no. 4 (1958): 697–701.
59. G. L. Guymon, "Summer Moisture-Temperature for Arctic Tundra," *ASCE Journal of the Irrigation and Drainage Division* 102, no. IR4 (1976): 403–411.
60. J. Weismüller, U. Wollschläger, J. Boike, X. Pan, Q. Yu, and K. Roth, "Modeling the Thermal Dynamics of the Active Layer at Two Contrasting Permafrost Sites on Svalbard and on the Tibetan Plateau," *The Cryosphere* 5, no. 3 (2011): 741–757, <https://doi.org/10.5194/tc-5-741-2011>.
61. L. He and Y. Tang, "Soil Development along Primary Succession Sequences on Moraines of Hailuoguo Glacier, Gongga Mountain, Sichuan, China," *Catena* 72, no. 2 (2008): 259–269, <https://doi.org/10.1016/j.catena.2007.05.010>.
62. J. G. Bockheim, A. V. Lupachev, H.-P. Blume, M. Bölter, F. N. B. Simas, and M. McLeod, "Distribution of Soil Taxa in Antarctica: A Preliminary Analysis," *Geoderma* 245–246 (2015): 104–111.
63. N. G. Midgley, T. N. Tonkin, D. J. Graham, and S. J. Cook, "Evolution of High-Arctic Glacial Landforms During Deglaciation," *Geomorphology* 311 (2018): 63–75, <https://doi.org/10.1016/j.geomorph.2018.03.027>.
64. S. Tavakoli, G. Gilbert, A. O. K. Lysdahl, R. Frauenfelder, and C. S. Forsberg, "Geoelectrical Properties of Saline Permafrost Soil in the Adventdalen Valley of Svalbard (Norway), Constrained With In-Situ Well Data," *Journal of Applied Geophysics* 195, no. September (2021): 104497, <https://doi.org/10.1016/j.jappgeo.2021.104497>.
65. T. Watanabe, N. Matsuoka, and H. H. Christiansen, "Mudboil and Ice-Wedge Dynamics Investigated by Electrical Resistivity Tomography, Ground Temperatures and Surface Movements in Svalbard," *Geografiska Annaler. Series a, Physical Geography* 94, no. 4 (2012): 445–457, <https://doi.org/10.1111/j.1468-0459.2012.00470.x>.
66. M. K. Woo and Z. Xia, "Effects of Hydrology on the Thermal Conditions of the Active Layer," *Nordic Hydrology* 27, no. 1–2 (1996): 129–142, <https://doi.org/10.2166/nh.1996.0024>.
67. C. A. Burga, B. Krüsi, M. Egli, et al., "Plant Succession and Soil Development on the Foreland of the Morteratsch Glacier (Pontresina, Switzerland): Straight Forward or Chaotic?" *Flora* 205 (2010): 561–576.
68. A. Dümig, R. Smittenberg, and I. Kögel-Knabner, "Concurrent Evolution of Organic and Mineral Components During Initial Soil Development after Retreat of the Damma Glacier, Switzerland," *Geoderma* 163 (2011): 83–94.
69. L. Hinzman, D. Kane, R. Gieck, and K. Everett, "Alaskan Arctic, Cold Regions," *Engineering* 19, no. 19 (1991): 95–110.
70. W. C. Oechel, G. L. Vourlitis, S. J. Hastings, R. P. Ault, Jr., and P. Bryant, "The Effects of Water Table Manipulation and Elevated Temperature on the Net CO₂ Flux of Wet Sedge Tundra Ecosystems," *Global Change Biology* 4, no. 1 (1998): 77–90.
71. J. Bradley, S. Arndt, M. Sabacká, et al., "Microbial Dynamics in a High Arctic Glacier Forefield: A Combined Field, Laboratory, and Modelling Approach," *Biogeosciences* 13 (2016): 5677–5696.
72. H. Y. Kwon, J. Y. Jung, O. S. Kim, D. Laffly, H. S. Lim, and Y. K. Lee, "Soil Development and Bacterial Community Shifts along the Chronosequence of the Midtre Lovénbreen Glacier Foreland in Svalbard," *Journal of Ecology and Environment* 38, no. 4 (2015): 461–476, <https://doi.org/10.5141/ecoenv.2015.049>.
73. Y. J. Kim, D. Laffly, S. E. Kim, et al., "Chronological Changes in Soil Biogeochemical Properties of the Glacier Foreland of Midtre Lovénbreen, Svalbard, Attributed to Soil-Forming Factors," *Geoderma* 415 (2022): 115777, <https://doi.org/10.1016/j.geoderma.2022.115777>.

Supporting Information

Additional supporting information can be found online in the Supporting Information section.